

RSC Advances



This is an *Accepted Manuscript*, which has been through the Royal Society of Chemistry peer review process and has been accepted for publication.

Accepted Manuscripts are published online shortly after acceptance, before technical editing, formatting and proof reading. Using this free service, authors can make their results available to the community, in citable form, before we publish the edited article. This *Accepted Manuscript* will be replaced by the edited, formatted and paginated article as soon as this is available.

You can find more information about *Accepted Manuscripts* in the [Information for Authors](#).

Please note that technical editing may introduce minor changes to the text and/or graphics, which may alter content. The journal's standard [Terms & Conditions](#) and the [Ethical guidelines](#) still apply. In no event shall the Royal Society of Chemistry be held responsible for any errors or omissions in this *Accepted Manuscript* or any consequences arising from the use of any information it contains.

New Insight into the Effect of the Formation Environment of Fh on Its Structure and Property

Hui Liu,^{a*} Xiuling Li,^b Yan Wang,^a Xin Yang,^a Zhen zhen,^a Rufen Chen,^a Denglu Hou,^b and Yu Wei^{a*}

^aCollege of Chemistry and Material Science, Hebei Normal University, Shijiazhuang, 050024, China. E-mail: liuhuicn@126.com, weiyu@mail.hebtu.edu.cn.

Tel: +86 311 80787433

^bCollege of Physics Science and Information Engineering, Hebei Normal University, Shijiazhuang, 050024, China

Abstract

Ferrihydrite(Fh) is a naturally occurring nanoscale iron oxyhydroxide mineral. It is of great interest in soil science and environmental science due to its extremely high surface area and reactivity. In this work, Fh samples were prepared by three procedures (named Fh-1, Fh-2, and Fh-3). The formation of Fh-1 went through a pH change from acidic to neutral, and the formation of Fh-2 went through a pH change from alkaline to neutral, while Fh-3 was formed at a constant neutral pH. The three Fhs were characterized by high-resolution transmission electron microscopy (HRTEM), terahertz (THz) spectroscopy, nitrogen adsorption isotherms, and low-temperature magnetic techniques. All these techniques indicate that the microstructure and formation process of Fh are strongly coupled. More importantly, the differences of the three Fhs in microstructure are reflected not only in their bulk structure but also in their surface properties. The adsorption and degradation of azo dye Mordant Yellow 10 (MY10) on the three Fhs were investigated. On the one hand, comparing with Fh-1 and Fh-2, Fh-3 exhibits a high density of active site per area, which leads to a large adsorption capacity. On the other hand, a strong affinity between Fh-3 and MY10 results in a more irreversible adsorption and a low degradation rate. The results from current study shed new light on synergetic effects of porosity and the variations of local structure on photocatalysis by iron oxide particles.

Key words: ferrihydrite; preparation procedure; terahertz spectroscopy; magnetic property; adsorption; degradation

1. Introduction

Ferrihydrite (Fh), an important member of iron oxide family, is a naturally occurring nanoscale iron oxyhydroxide mineral. In the environmental science field, Fh serves as a scavenger of heavy metals and metalloids during the treatment of wastewaters and in remedial activities.^{1,2} It has been demonstrated to photocatalytically degrade and adsorb some organic pollutants^{3,4} and catalyze the decomposition of H₂O₂.² Moreover, Fh is also thought to play a significant role in geochemical processes of iron minerals.⁵ However, due to its small size and poor crystallinity, ferrihydrite is difficult to be identified and characterized explicitly in routine determinative procedures such as powder X-ray diffraction (XRD), Fourier transform infrared (FT-IR) and Raman-spectroscopy. Up to now, two models were used to describe its structure; one is developed by Drits et al.⁶ and the other is proposed by Michel et al.⁷ The main difference between both models is the multiphase character of Drits' model and the single-phase character of Michel's model. However, the results of Michel et al. were disputed by some researchers.⁸⁻¹⁰ Manceau pointed out that Michel's model is unrealistic because it violates Pauling's 2nd rule.⁹ After that, Michel et al. revised their previous defect-free structural model¹¹. Manceau found that Pauling's 2nd rule is no longer violated in the revised model, whereas a new problem has emerged, which is the violation of Pauling's 3rd rule¹². In our opinion, which model is more reasonable should be verified by more experimental data, as any proposed structure for Fh should be quantitatively consistent with the basic physico-chemical properties of the material.

Recently, our research area focuses on exploring the formation, transformation and properties of Fh.¹³⁻¹⁷ We prepared Fhs by three procedures at pH 9 and found that there are great differences in their reactivity. The transformation time from Fh-3 to hematite (about 1 h) is much shorter than that from the other two. The size of as-prepared hematite particles in Fh-3 system is not only smaller but also more uniform than that in the other two systems. XRD patterns indicate that both Fh-1 and Fh-2 are 2-line Fhs, but some peaks of hematite appear in Fh-3. We deduced that there probably exist some differences in their sub-microstructure for the three Fhs. In order to more deeply understand the correlation between structure and property of ferrihydrite, in this paper, we prepared the

three Fhs at pH 7 and their XRD patterns indicate that all the three samples are 2-line Fhs. The three samples were characterized by high-resolution transmission electron microscopy (HRTEM), terahertz (THz) spectroscopy, and low-temperature magnetic techniques *etc.* and some new information on structural differences was obtained. In addition, the three Fhs exhibit great differences in their adsorbing and degrading organic pollutant. More important, the results obtained in the present paper can be explained by Drits' multiphas model.

2. Experimental section

2.1 Materials

MY 10 was purchased from J&K and was used without further purification. Ferric chloride hexahydrate ($\text{FeCl}_3 \cdot 6\text{H}_2\text{O}$), sodium hydroxide (NaOH) and 30% hydrogen peroxide (H_2O_2) were purchased from Tianjin Kaitong. All these chemicals were analytical grade. A known dye concentration was prepared in deionized water and used as the stock solution for the study.

2.2 Synthesis of samples

Fh was prepared using the three different procedures described in our earlier paper.¹³ Briefly, Procedure 1 (**Fh-1**): NaOH solution (6.0 mol L^{-1}) was added dropwise to 50 mL of 1.0 mol L^{-1} ferric chloride solution until pH 7. Procedure 2 (**Fh-2**): the mixing procedure of Fe^{3+} and NaOH solutions is opposite to procedure 1. Procedure 3 (**Fh-3**): NaOH solution (6.0 mol L^{-1}) and 25 mL of 2.0 mol L^{-1} Fe^{3+} solution were added simultaneously into 40 mL of water until Fe^{3+} solution was exhausted. The rate of addition of the two solutions was controlled via peristaltic pump by maintaining pH 7 with an accuracy of better than 0.5 pH units. The above process was carried out under vigorous stirring at room temperature and the total volume was adjusted to 100 mL. The gels were collected, thoroughly washed with deionized water and dried at about $50 \text{ }^\circ\text{C}$.

2.3 Characterization of samples

High-resolution transmission electron microscopy (HRTEM) images were obtained using a JEOL 2010 microscope operating at 200 kV. The Brunauer-Emmett-Teller (BET) specific surface area and the Barrett-Joyner-Halenda (BJH) pore size distribution were

measured using a Micromeritics ASAP 2020 apparatus. THz spectra were acquired on a TPITM spectra 1000 transmission spectrometer (TeraView Limited, Cambridge, UK). Samples were measured at an instrument resolution of 2-3 cm^{-1} over the range of 0-3 THz, corresponding 0-100 cm^{-1} . The magnetic properties measurements were performed using a physical property measurement system (PPMS-9).

2.4 Adsorption performance measurements

Adsorption of MY10 on the Fh was determined in the dark. A fixed amount of the Fh (0.0250 g) was added to 50 mL of MY10 solution with varying concentrations in Pyrex cylindrical reactor vessels. These were agitated for 1 h and maintained at a temperature of 288 K. The concentrations of MY10 were measured by a UV-vis 752 spectrophotometer.

2.5 Photochemical performance measurements

All photoreaction experiments were carried out in a photochemical reactor system, which consist of a Pyrex cylindrical reactor vessel with an effective volume of 250 mL, a cooling water jacket and an 8 W ultraviolet light lamp as a UV light source. The reaction temperature was kept at 288 K. The reaction suspension was prepared by adding given 0.1000 g of Fh powders to 200 mL of MY10 solution. Prior to irradiation, the suspensions were magnetically stirred in the dark for 60 min to establish the adsorption/desorption equilibrium between MY10 and Fh particles. H_2O_2 was added to the reaction vessel at the beginning of the irradiation. At given irradiation time intervals, about 10 mL aliquots were sampled, centrifuged, and subsequently filtered through a 0.22 μm Millipore filter to remove Fh. The concentration of MY10 in filtrate was analyzed by UV-Visible spectrophotometer at a wavelength of 354 nm.

3. Results and Discussion

3.1 Structure characterization of Fhs

XRD patterns (not shown here) of the three samples yields two broad and weak diffraction peaks, suggesting all of them are 2-line Fh. Their TEM, HRTEM images and SAED patterns are shown in Fig. 1. The different degree of aggregate was observed from Figs. a₁, b₁ and c₁. Under the same condition, the scattered degree of Fh-3 is better than that of the other two. HRTEM images show single spherical particles, ca. 2-5 nm in size.

Primary Fh particles with lattice fringes were detectable in all Fhs at the highest magnification. Widely scattered areas that have distinct lattice fringes are surrounded by areas without recognizable fringes, which can also be produced by crystallites that are not in appropriate orientations or are superposed on each other. Fh-3 differs mainly from Fh-1 and Fh-2 in that it exhibits smaller, more uniform and compact particles. Crystal faces of the hexagonally shaped particles could be observed in Fh-3 system (Fig. 1c, arrow). The SAED patterns of Fhs show two bright rings and each of which has a shoulder, indicating that Fhs are characterized by small crystal size and/or low structural order. Differences in SAED pattern among the three Fhs were small. All features are in line with 2-line Fh.¹⁸

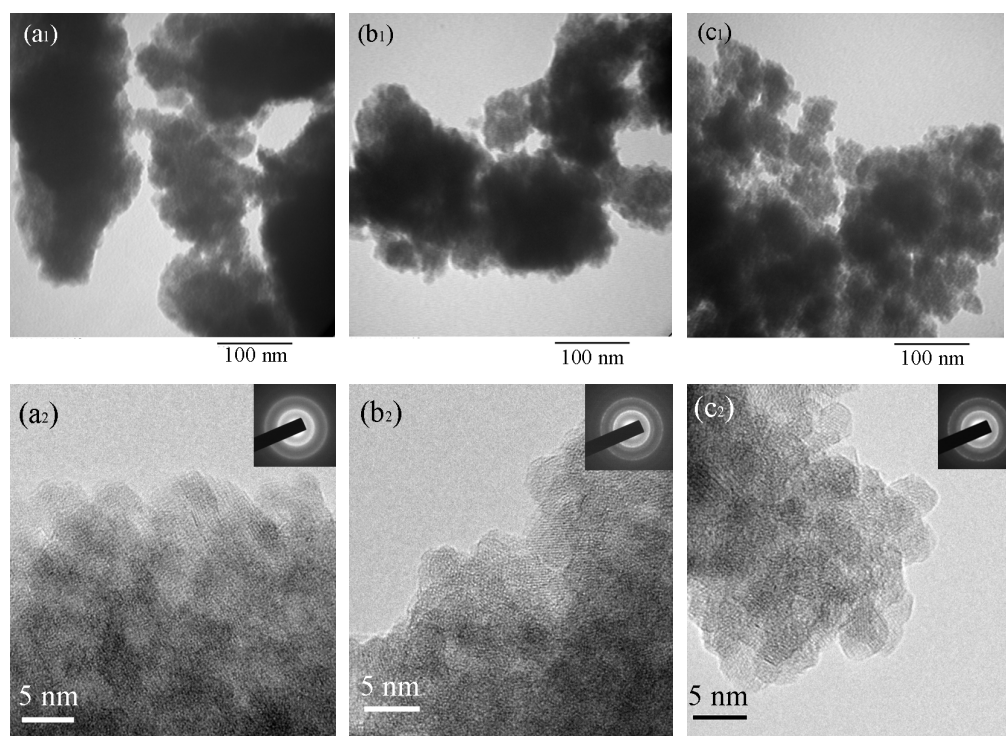


Fig. 1 TEM, HRTEM images and SAED patterns of the three samples a: Fh-1; b: Fh-2; c: Fh-3; Arrow points at hexagonally shaped crystals.

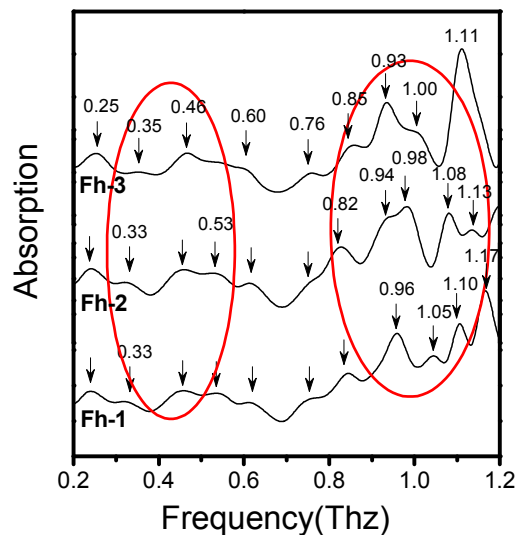


Fig. 2 THz spectra of the three Fhs

Due to the ability of THz spectroscopy to clearly distinguish between samples with good and poor long range order and other changes in intermolecular bonding networks, it is a powerful technique for the study in condensed systems.¹⁹ Work in this area has already demonstrated the potential for THz spectroscopy as a useful addition to other solid state techniques such as DSC and XRD *etc.*^{20,21} An overlay of the THz spectra for the three Fhs was shown in Fig. 2. The main differences in THz spectra for the three Fhs focus on two bands from 0.3 to 0.6 and from 0.8 to 1.2. For example, in Fh-1 and Fh-2, the peaks at 0.33 and 0.53 THz were observed, while in Fh-3, not the two peaks but 0.35 THz was occurred. Although we cannot carry out a theoretical calculation to predict the THz spectroscopy of the three Fhs due to its complicated structure, from the results in THz spectra, we daringly concluded that there are some differences in their microstructure. This difference will be confirmed further by the magnetic property data at low temperatures.

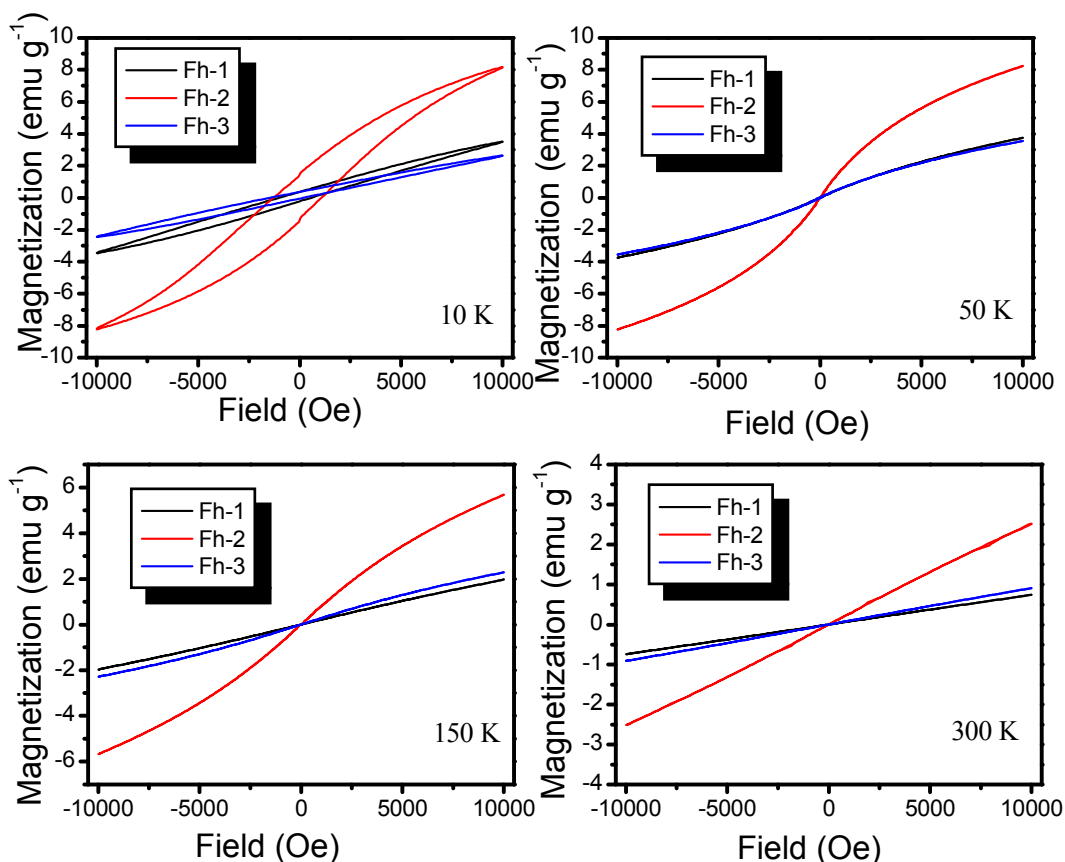


Fig. 3 Magnetic hysteresis data of the three samples obtained on PPMS for temperatures ranging from 10 to 300 K.

Magnetic characterization of the three samples consisted of a series of measurements on dry powders using a Physical Properties Measurement System (Fig. 3). Hysteresis loops were not saturated by the maximum field of 10000 Oe. This behavior has also been reported by Guyodo et al²², who inferred that Fh was an antiferromagnet with a small ferromagnetic-like moment. This small moment could arise from uncompensated spins present either inside or at the surface of the particles. At 10 K, remanent magnetizations are 0.3026, 1.4262 and 0.2201 emu/g, and coercivities are 793.93, 1182.08 and 811.65 Oe for Fh-1, Fh-2 and Fh-3, respectively. Hysteresis is progressively suppressed upon warming to room temperature. The shape of the curves remains sigmoidal after unblocking occurred. Above ordering temperature, the plots should be linear. Our measurements indicate that the actual ordering temperature is at about 150 K for Fh-3, higher than 150 K for Fh-2, and lower than 150 K for Fh-1. A progressive decrease in coercivity and a gradual change in the curvature of the hysteresis

curves with elevated temperature are observed in the data, indicating that the phenomenon is related to the uncompensated moments. As seen in the hysteresis data, all three samples display typical superparamagnetic behavior at room temperature.

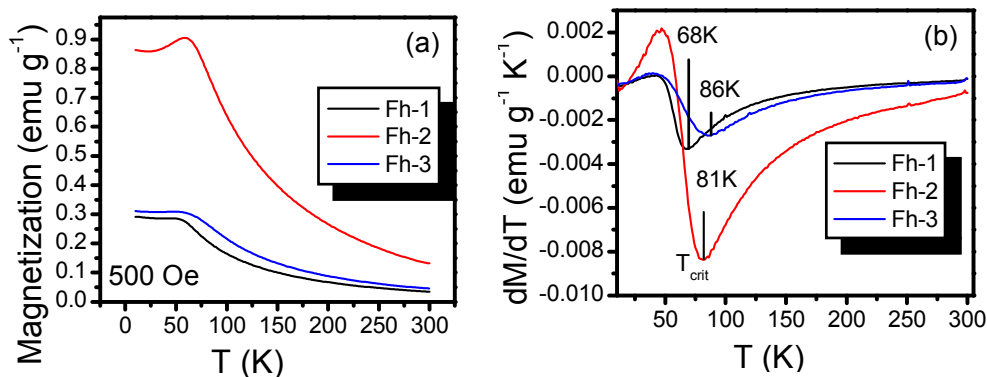


Fig. 4 $M \sim T$ (a) and $dM/dT \sim T$ (b) curves of the three Fhs

Fig. 4a shows the zero-field cooled (ZFC) magnetization M , as a function of temperature T , in the temperature range 10-300 K at 500 Oe for the samples. For ZFC the samples were cooled in the absence of an external magnetic field, which was applied then at 10 K. The samples undergo a paramagnetic to ferromagnetic transition at Curie as the temperature decreases. The magnetic transition temperatures have been determined from the minima in the dM/dT plots²³ as shown in Fig. 4b. While at lower temperatures below (T_{crit}) a secondary transition started to become visible. This transition as shown is characterized by the further increases of magnetization and is due to magnetic frustration. The origin of this magnetic frustration in Fh is more probably linked to the incoherent displacements of the oxygen atoms bonded to Fe-cations. The data in Fig. 4b show that T_{crit} is 68, 81 and 86 K for Fh-1, Fh-2 and Fh-3, respectively. The difference in T_{crit} of the three Fhs is related to the degree of distortion relative to a perfect Fe-O_6 octahedra. "Distortion" here refers to the geometric arrangement of chemical bonds around the Fe ion. Analogous phenomenon has been reported by Chernyshova et al.²⁴ They characterized the structure and morphology of hematite particles with different sizes and found that hematite nanoparticles possess maghemite-like defects and the net lattice disorder in the near surface regions. Both thermodynamical and kinetic factors influence the structure of hematite nanoparticles. Based on the above analysis and experimental data, we consider that two reasons give rise to above results. The first reason is due to the

formation environment of Fh. The formation of Fh-1 went through a pH change from acidic (about pH 0.8) to neutral (pH 7). In this process, a three-step hydrolysis process occurs consisting of formation of low-molecular-weight species (e.g. $\text{Fe}(\text{OH})^{2+}$, $\text{Fe}(\text{OH})_2^+$ and dimeric $\text{Fe}_2(\text{OH})_2^{4+}$), the polymer spheres from low-molecular-weight species, and subsequent precipitation (Fh). The formation process of Fh-3 was completed at a constant pH 7 which is larger than the initial pH to form Fh precipitate. That is, not those low-molecular-weight species but Fh precipitate directly form. The similar situation happens in Fh-2 system. The second reason is due to microstructure of Fh. According to the data of Drits et al.,⁶ Fh is a multiphase material which comprises three components, f-phase, d-phase and subordinate ultradisperse hematite. The proportions of three components in the three Fhs are different.¹³ Thus, ferromagnetic coupling in the three Fhs is also different, which leads to the above result (Fig. 4b).

In addition, according to multiphase model of Fh, there are cavities or channels in its f-phase.^{6,9} The pores in Fh comprises two types, structural cavities or channels in the f-phase and interparticle spaces in the aggregates of Fh nanoparticles. Different type of pore is associated with a characteristic type of adsorption isotherm.²⁵ Fig. 5 presents nitrogen adsorption–desorption isotherms and BJH pore size distribution of the three Fhs and Table 1 shows the BET specific surface area, t-plot micropore area, and average pore diameter of the three samples. Fh-1 has a surface area of $277.4 \text{ m}^2 \text{ g}^{-1}$ of which 44.7% is pore surface area (Table 1). It displays a type I isotherm, indicating a high adsorption energy at low saturation and microporosity. Fh-2 has a surface area of $268.1 \text{ m}^2 \text{ g}^{-1}$ of which 24.8% is pore surface area. Its isotherm displays type IV curves with a hysteresis loop, indicating a mesoporous structure. The pore size distribution for Fh-2 exhibits a maxima at ca. 3.7 and 1.8 nm, respectively. The hysteresis observed in Fh-2 is of a type H_4 loop (according to the IUPAC classification). Fh-3 displays both type II and IV isotherms. Type II isotherm is associated with a nonporous or mesoporous sample. Our earlier results indicated that the proportion of f-phase in Fh-3 is the least.¹³ The hysteresis observed in Fh-3 is of a type H_3 loop. Fig. 5 reveals that the micropore (pore size less than 2.0 nm) volume in Fh-3 is much less than that in Fh-1. Although 16.3% of the total surface area is pore surface area in Fh-3, most pores fall into the size range of mesopores,

which should be attributed to interparticle pores. In fact, the pretreatment conditions for the three samples are completely identical in this study. The different porous structures possibly provide more accessible active sites and enhanced catalytic activity.

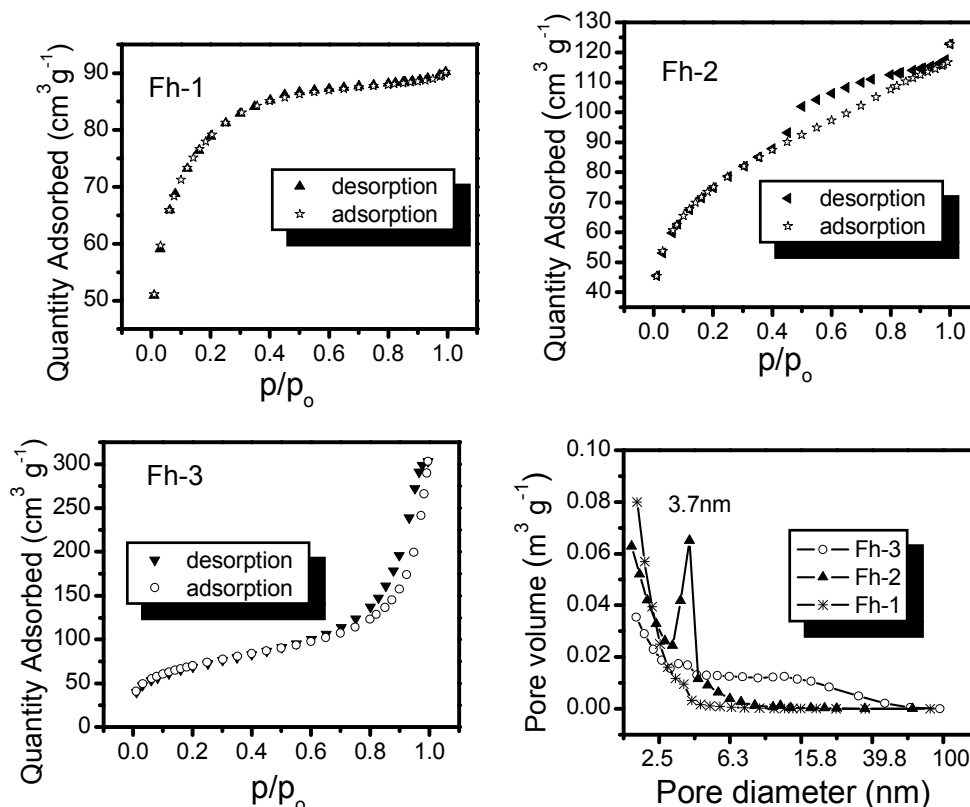


Fig. 5 Nitrogen adsorption–desorption isotherms and BJH pore size distribution of the three Fhs

Table 1 BET specific surface area, t-plot micropore area and average pore diameter of the three Fh samples

Sample	Fh-1	Fh-2	Fh-3
BET specific surface area /m ² g ⁻¹	277.4	268.1	252.4
t-plot micropore area /m ² g ⁻¹	124.2	66.5	41.2
t-plot external surface area /m ² g ⁻¹	153.3	201.6	211.1
BJH adsorption average pore diameter /nm	2.7	3.6	10.1
BJH desorption average pore diameter /nm	2.5	3.1	9.8

3.2 Absorption property of three Fhs

The adsorption of MY10 on the three Fhs was studied and their adsorption isotherms at 288 K, obtained by plotting c_e/Γ versus c_e , are shown in Fig. 6. These are well fitted by the Langmuir adsorption model given by Eq. (1).

$$\frac{c_e}{\Gamma} = \frac{1}{\Gamma_{\max}} \cdot c_e + \frac{1}{K_a \cdot \Gamma_{\max}} \quad (1)$$

Where K_a the adsorption equilibrium constant in L mol^{-1} and Γ_{\max} is the saturated adsorption capacity in mol g^{-1} . The values of Γ_{\max} and K_a are listed in Table 2. Both Γ_{\max} and K_a are ranked in the order of Fh-3>Fh-2>Fh-1, while the BET specific surface area followed the order Fh-1>Fh-2>Fh-3, suggesting that the adsorption capacity of MY10 on the three Fhs doesn't depend entirely on their specific surface area.

To further understand the differences in the adsorption property of the three Fhs, the dimensionless separation factor R_L was used to predict the affinity between the sorbate and adsorbent as well as adsorption reversibility.²⁶

$$R_L = \frac{1}{1 + c_0 K_a} \quad (2)$$

Where K_a is the Langmuir constant in L mol^{-1} and c_0 is the initial concentration of MY10 in mol L^{-1} . The values of R_L , classified as $R_L > 1$, $0 < R_L < 1$ and $R_L = 0$, suggests that adsorption is unfavorable, favorable and irreversible, respectively. The values of R_L for adsorption of MY10 on to the three Fhs have been calculated and shown in Table 2. Obviously, all the three R_L values lie between 0 and 1, indicating that the adsorption of MY10 on the three Fhs is favorable. However, some subtle differences can be observed for the R_L values. The R_L value of Fh-3 is much less than those of Fh-1 and Fh-2. Moreover, the R_L value of Fh-3 is close to zero, which probably means that the adsorption of MY10 on Fh-3 is more irreversible, comparing with Fh-1 and Fh-2. In other words, the affinity between Fh-3 and MY10 is larger than that of the other two samples.

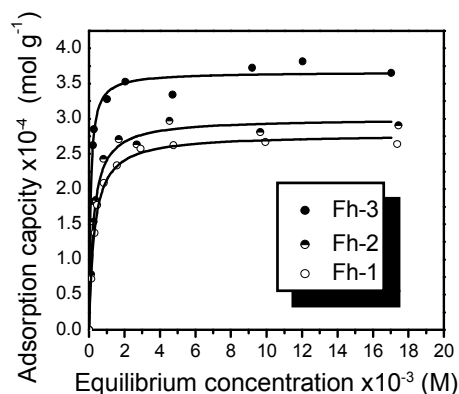


Fig. 6 The adsorption isotherms of MY10 on the surface of the three Fhs by plotting the equilibrium concentration (c_e) vs. the adsorbed capacity of MY10 (I)

Table 2 The saturated adsorption capacity (I_{max}) and the adsorption equilibrium constant (K_a) of MY10

Sample	$I_{max} \times 10^{-4} / \text{mol g}^{-1}$	$K_a \times 10^5 / \text{L mol}^{-1}$	R_L	R^2
Fh-1	2.78	0.33	0.1306,	0.993
Fh-2	3.00	0.41	0.1087	0.988
Fh-3	3.66	1.14	0.0420	0.991

3.3 Degradation of MY10 on three Fhs

To ensure the establishment of adsorption/desorption equilibrium, the Fh/MY10 dispersion was stirred in the dark for 60 min before UV irradiation. The results indicated that 87 % of MY10 was adsorbed on Fh-3 during the process of adsorption/desorption equilibrium while only about 50 % of MY10 was adsorbed on Fh-1 and Fh-2 under the same conditions. It is known that the large specific surface area and total pore volume would be beneficial to achieve better physical adsorption.²⁷ Although BET surface area of Fh-3 is not the largest, its external surface area is the largest. The reasonable explanation should be that the adsorption of MY10 on Fh aggregate mainly occurs on its external surface because molecules of MY10 are too large to enter into the cavities or nanoporosity existing in the f-phase of the Fh structure. Fig. 7a shows the change of degradation rate of MY10 with irradiation time in the presence of Fh and H₂O₂ under UV irradiation. Of the three systems, the degradation rate of MY10 in the Fh-3 system is

75.1 %, while the degradation rates of MY10 in Fh-1 and Fh-2 systems are 89.24 % and 93.4 %, respectively. Actually, after establishment of adsorption/desorption equilibrium, the concentration of MY10 in solution in Fh-3 system is much lower than those in Fh-1 and Fh-2 systems due to the higher adsorption capacity of Fh-3, which leads to low initial concentration of MY10 in Fh-3 system at the beginning of degradation. To compare the catalytic activity of the three Fhs on the same scale, the concentration of MY10 in the Fh-3 system after the adsorption/desorption equilibrium was adjusted according to the value of the concentration of MY10 in Fh-1 system. The degradation rate of MY10 was again determined. The result given in Fig. 7b shows that the degradation rate was not increased. This result is related to the high affinity between Fh-3 and MY10. Though more MY10 molecules are easily adsorbed on to the surface of the Fh-3 aggregates, it is more difficult for them to be desorbed from Fh-3 aggregates due to irreversible adsorption of MY10 (Table 2), which retards the re-adsorption and degradation of the MY10 in solution.

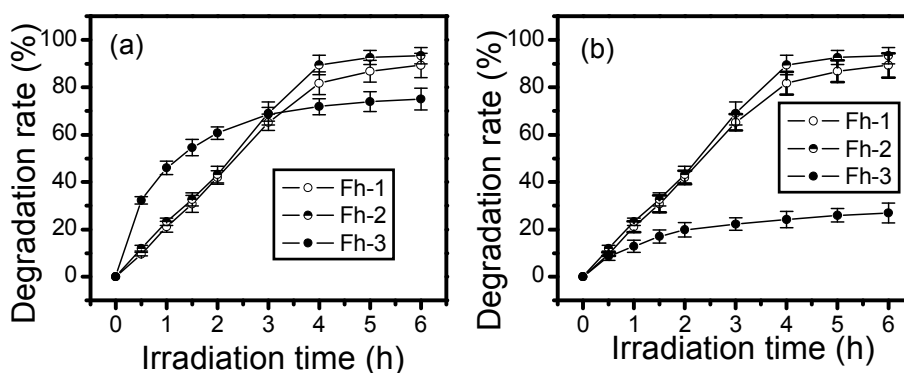


Fig. 7 Degradation rate of MY10 vs. irradiation time before (a) and after (b) the concentration of MY10 in solution in Fh-3 system was adjusted.

Usually, dye degradation by H_2O_2 promotion mainly occurs on the surface of iron oxide photocatalysts rather than in solution bulk.²⁸ The effects of H_2O_2 in enhancing the photocatalytic performance of catalysts is ascribed to two aspects.²⁹ One is conduction electron scavenging and the other is the Fenton-like reaction. When visible light illuminates iron oxides, charge carriers (e.g. electrons and holes) are generated.



There are two pathways to annihilate the electrons. Firstly, H_2O_2 directly traps electrons to form $\text{OH}\cdot$. Secondly, Fe^{3+} on the surface of iron oxides traps electrons to transform Fe^{2+} and then Fe^{2+} reacts with H_2O_2 to form $\text{OH}\cdot$. Moreover, iron oxide can catalyze the decomposition of hydrogen peroxide to produce $\text{OH}\cdot$ even under darkness.³⁰ Bahnemann et al proposed that physical properties of a photocatalyst such as crystal structure, surface area, size distribution, porosity, and band gap determine its reactivity.³¹

To compare the degradation nature of the three Fhs on the same scale, the adsorption capacity of the three Fhs was normalized to their surface area. The calculated ratio of the adsorption capacity per unit surface area is 1.00:1.08:1.81 for Fh-1, Fh-2 and Fh-3, respectively, suggesting that the number of active sites per unit surface area (i.e. the density of active site per area) on Fh-3 is the largest of the three Fhs. The rate constants for the decomposition of H_2O_2 has been determined using the three Fhs as catalysts and they are ranked in the order $k_{\text{Fh-1}} < k_{\text{Fh-3}} < k_{\text{Fh-2}}$.¹³ Based on the above information, the differences in the degradation rate of MY10 for the three Fhs can be understood. For the sake of convenience, Fig. 8 presents the sketch of the degradation mechanism of MY10 in ferrihydrite/ H_2O_2 system.

As for Fh-3, the adsorption of MY10 occurs not only on its external surface but also on its mesopore surface due to large pore diameter (Table 1). Although MY10 molecules occupy most active sites after the adsorption/desorption equilibrium, it is impossible for all of the active sites to be occupied by MY10 molecules due to steric hindrance. When visible light and H_2O_2 are introduced into the system, only those Fe(III) sites unoccupied by MY10 contribute to the formation of $\text{OH}\cdot$. The experimental fact is that not only is the micropore area of Fh-3 very small but also the adsorption density per area of MY10 on Fh-3 is very high. A high adsorption density of MY10 is unfavorable for the generation of charge carriers (equation 3). Meanwhile, it hinders H_2O_2 entering the micropores to be catalytically decomposed. The two factors mentioned above lead to a slow catalytic degradation rate of MY10. Moreover, from its R_L value (Table 2), the adsorption of MY10 on the surface of Fh-3 is more irreversible so that the degraded MY10 molecules are hard to be desorbed from the surface of Fh-3, which also contributes to the low

degradation efficiency in the Fh-3 system (Fig. 8). As for Fh-1, the adsorption of MY10 mainly occurs on its external surface. On the one hand, it is difficult for MY10 molecules to enter into the cavities or channels existing in the f-phase of the Fh structure¹³ due to its large molecule size (The length of MY 10 anion is 1.294 nm³²). On the other hand, it is also difficult for MY10 molecules to enter into the interparticle micropores due to small micropore diameter (Table 2) and steric hindrance. However, the low density of active site per unit area for Fh-1 is favorable both for reaction 3 and for the catalytic decomposition of H₂O₂, which leads to more OH• generated and a fast degradation efficiency in the Fh-1 system. Moreover, from the R_L value, the adsorption of MY10 on the surface of Fh-1 is more reversible, comparing with Fh-3. The degraded MY10 molecules desorb from the surface of Fh-1 more easily than Fh-3. After the degraded MY10 molecules leave the surface of Fh, MY10 molecules in the bulk solution were again adsorbed, which makes the adsorption-degradation-desorption process occur continuously and more MY10 molecules are degraded. The situation in Fh-2 system should be similar to that in Fh-1 system.

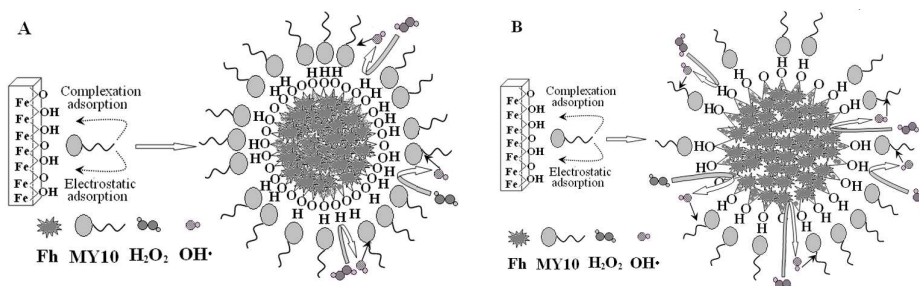


Fig. 8 The sketch of the degradation mechanism of MY10 in ferrihydrite/H₂O₂ system.

A: Fh-3, B: Fh-1 and Fh-2

In order to further confirm the conclusion above, the effect of the concentration of H₂O₂ on the degradation of MY10 in the three systems was determined and the results are shown in Fig. 9. As shown in Fig. 9, the oxidation rate increased with the increase of H₂O₂ concentration. Almost all the MY10 was oxidized in the presence of Fh-1 or Fh-2 with 3 and 5 mmol L⁻¹ H₂O₂ after a reaction time of 6 h. These results are in contrast to the Fh-3 / H₂O₂ system where the oxidation rate of MY10 was only 67% in the presence of 5 mmol L⁻¹ H₂O₂ after 6 h irradiation. The higher adsorption density of MY10 on the

Fh-3 surface, the smaller micropore area within the Fh-3 aggregate and the higher degree of irreversible adsorption are all responsible for this result.

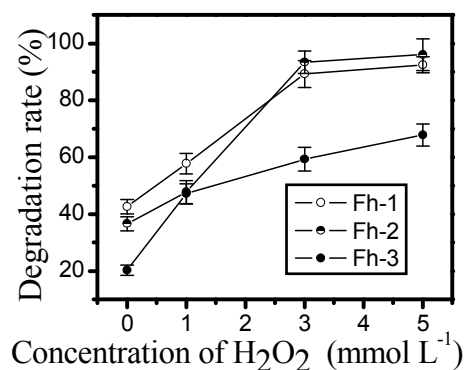


Fig. 9 Effects of the concentration of H₂O₂ on the degradation of MY10

4. Conclusions

Fh samples, prepared by three approaches, were characterized by HRTEM, THz, nitrogen adsorption isotherms, and low-temperature magnetic techniques. The results indicate that the microstructure and formation process of Fh are strongly coupled. The photocatalytic activity toward azo MY10 in the presence of trace H₂O₂ by the three Fhs is porosity-, surficial and local structure-dependent. The total surface area of the three Fhs are ranked in the order Fh-1>Fh-2>Fh-3, while the saturated adsorption capacity of the three Fhs was inversely proportional both to specific surface area and to degradation ratio. Comparing with Fh-1 and Fh-2, a high adsorption density and a small micropore surface area in Fh-3 system are unfavorable for the generation of OH•, which results in a low degradation rate. At the same time, the irreversible adsorption of MY10 on Fh-3 is also unfavorable for the degradation of MY10. The results from current study shed new light on synergetic effects of porosity and the variations of local structure on photocatalysis by iron oxide particles.

Acknowledgments

The authors are grateful to the National Natural Science Foundation of China (21277040, 21077031) and Hebei Province (B2012205041). The authors thank International Science Editing for editing the manuscript.

References

- 1 E. M. Moon and C. L. Peacock, *Geochim. Cosmochim. Acta*, 2012, **92**, 203-219.
- 2 J. Filip, R. Zboril, O. Schneeweiss, J. Zeman, M. Cernik, P. Kvapil and M. Otyepka, *Environ. Sci. Technol.*, 2007, **41**, 4367-4374.
- 3 K. Hanna and C. Carteret, *Chemosphere*, 2007, **70**, 178–186.
- 4 J. C. Barreiro, M. D. Capelato, L. Martin-Neto and H. C. B. Hansen, *Water Res.*, 2007, **41**, 55-62.
- 5 C. M. Hansel, D. R. Learman, C. J. Lentini and E. B. Ekstrom, *Geochim. Cosmochim. Acta*, 2011, **75**, 4653-4666.
- 6 V. A. Drits, B. A. Sakharov,, A. L. Salyn and A. Manceau, *Clay Miner.*, 1993, **28**, 185–207.
- 7 F. M. Michel, L. Ehm, S. M. Antao, P. L. Lee, P. J. Chupas, G. Liu, D. R. Strongin, M. A. A. Schoonen, B. L. Phillips and J. B. Parise, *Science*, 2007, *316*, 1726-1729.
- 8 D. G. Rancourt and J. F. Meunier, *Am. Mineral.*, 2008, *93*, 1412-1417.
- 9 A. Manceau, *Clay Miner.*, 2009, *44*, 19–34.
- 10 T. Hiemstra and W. H. Van Riemsdijk, *Geochim Cosmochim Acta*, 2009, *73*, 4423–4436.
- 11 F. M. Michel, V. Barron, J. Torrent, M. P. Morales, C. J. Serna, J.-F. Boily, Q. Liu, A. Ambrosini, A. C. Cismasu and G. E. Brown Jr., *PNAS*, 2010, *107*, 2787–2792.
- 12 A. Manceau, *Clay Miner.*, 2010, *45*, 225–228.
- 13 H. Liu, Y. Wang, Y. Ma and Y. Wei, *Chemosphere*, 2010, *79*, 802–806.
- 14 H. Liu, P. Li, B. Lu, Y. Wei and Y. H. Sun, *J. Solid State Chem.*, 2009, *182*, 1767–1771.
- 15 S. Meng, H. Liu, C. H. Yang, Y. Wei and D. L. Hou, *Appl. Surf. Sci.*, 2012, *258*, 4449–4454
- 16 Y. Ma, S. Meng, M. Qin, H. Liu and Y. Wei. *J. Phys. Chem. Solids*, 2012, *73*, 30–34.
- 17 M. R. Ma, L. J. Yang, Q. Liu, H. Liu and Y. Wei, *Acta Phys. Chim. Sin.*, 2008, *24*, 2282–2286.
- 18 D. E. Janney, J. M. Cowley and P. R. Buseck, *Am. Mineral.* 2000, **85**, 1180–1187.

- 19 S. G. Chou, P. E. Stutzman, S. Z. Wang, E. J. Garboczi, W. F. Egelhoff and D. F. Plusquellic, *J. Phys. Chem. C*, 2012, **116**, 16161–16166.
- 20 A. I. McIntosh, B. Yang, S. M. Goldup, M. Watkinson and R. S. Donnan, *Chem. Soc. Rev.*, 2012, **41**, 2072–2082.
- 21 J. G. Han, B. K. Woo, W. Chen, M. Sang, X. C. Lu and W. L. Zhang, *J. Phys. Chem. C*, 2008, **112**, 17512–17516.
- 22 Y. Guyodo, S. K. Banerjee, R. L. Penn, D. Burleson, T. S. Berquo, T. Seda and P. Solheid, *Phys. Earth Planet. In.*, 2006, **154**, 222-233.
- 23 S. Asthana, D. Bahadur, A. K. Nigam and S. K. Malik, *J. Phys.: Condens. Mat.*, 2004, **16**, 5297–5307.
- 24 I. V. Chernyshova M. F. Hochella Jr and A. S. Maddenc, *Phys. Chem. Chem. Phys.*, 2007, **9**, 1736–1750.
- 25 R. M. Cornell and U. Schwertmann, *The Iron Oxides*, Second ed., WILEY-VCH, New York, 2003 pp. 533.
- 26 A. Bhatnagar and A.K. Jain, *J. Colloid Interf. Sci.*, 2005, **281**, 49–55.
- 27 F. B. Li, X. Z. Li, M. F. Hou, K. W. Cheah and W. C. H. Choy, *Appl. Catal. A* 2005, **285**, 181–189.
- 28 W. Du, Y. Xu, Y. Wang, *Langmuir* 2008, **24**, 175–181.
- 29 X. M. Zhou, H. C. Yang, C. X. Wang, X. B. Mao, Y. S. Wang, Y. L. Yang, and G. Liu, *J. Phys. Chem. C*, 2010, **114**, 17051–17061.
- 30 S. S. Lin and M. D. Gurol, *Environ. Sci. Technol.*, 1998, **32**, 1417–1423.
31. D. W. Bahnemann, In photochemical conversion and storage of solar energy; Pelizzetti, E., Schiavello, M., Eds.; Kluwer Academic Publishers: Dordrecht, 1991; p 251.
- 32 M. Pu, Y. H. Liu, L. Y. Liu, X. Z. Dong, J. He and D. G. Evans, *J. Phys. Chem. Solids*, 2008, **69**, 1084–1087.